Available online at www.sciencedirect.com
SCIENCE DIRECT
Journal of Catalysis 239 (2006) 83–96
JOURNAL OF CATALYSIS
www.elsevier.com/locate/jcat

The role of nanostructure in nitrogen-containing carbon catalysts for the oxygen reduction reaction

Paul H. Matter, Ling Zhang, Umit S. Ozkan *

The Ohio State University, Department of Chemical Engineering, 140 W. 19th Ave, Columbus, OH 43210, USA

Received 19 November 2005; revised 13 January 2006; accepted 20 January 2006

Available online 10 February 2006

Abstract

Catalysts for the oxygen reduction reaction (ORR) were prepared by the high-temperature pyrolysis of acetonitrile over Vulcan carbon XC-72, and Vulcan carbon impregnated with 2 wt% Fe or 2 wt% Ni in the form of an acetate salt. The catalysts were characterized by BET surface area analysis, BJH pore size distribution, electrical conductivity testing, transmission electron microscopy (TEM), temperature-programmed oxidation, thermogravimetric analysis, X-ray diffraction, X-ray photoelectron spectroscopy, and rotating disk electrode half-cell testing. The most active catalysts were formed when Fe was added to the support before the pyrolysis; however, samples in which Ni or no metal was added still showed increased activity for oxygen reduction compared with untreated carbon. The most active catalyst had a significantly higher amount of pyridinic nitrogen, as determined from XPS. A hypothesis has been proposed to explain this trend based on the formation of different nanostructures depending on which support material is used for the acetonitrile decomposition. According to this proposed explanation, nitrogen-containing carbon samples with nanostructures resulting in exposure of more edge planes (the plane in which pyridinic nitrogen is found) will be more active for the ORR. TEM images of the samples strongly support this hypothesis. Further research is needed to positively identify the active site for oxygen reduction; however, this site is likely located on carbon edge planes.

Keywords: PEM fuel cells; Oxygen reduction; Nitrogen-containing carbon; Carbon nanostructure

1. Introduction

Fuel cells offer a potentially cleaner and more efficient source of energy compared with internal combustion engines and other energy-conversion devices. Proton-exchange membrane (PEM) fuel cells are a type of fuel cell currently under consideration for use in mobile applications, because their low operating temperature allows for quick start-ups compared with other fuel cells. Currently, a major limitation to the commercialization of PEM fuel cells is the high cost of their components. For example, the electrodes of PEM fuel cells require Pt to catalyze the low-temperature reactions. Pt is expensive, and its sparse availability could limit the commercial application of PEM fuel cells [1].

The cathode of the fuel cell is the electrode where oxygen is reduced to water by the following reaction, known as the oxygen reduction reaction (ORR):

$$O_2 + 4H^+ + 4e^- \rightarrow 2H_2O \quad (1.23\ \text{V vs. NHE at STP [2]}).$$

Even when Pt is used as a catalyst, this reaction is relatively slow and requires a large overpotential before reaction kinetics increase, thus decreasing the efficiency and maximum power of the cell. Consequently, developing alternative catalysts to Pt for the ORR in PEM fuel cells is a major goal for researchers and a necessity for the commercialization of fuel cells.

Over the past several decades, researchers have investigated organic macrocycles, such as metalloporphyrins, for use as cathode catalysts [3–17]. These molecules are similar to the active site for oxygen adsorption in hemoglobin, where oxygen is adsorbed on an iron center stabilized by the nitrogen functional groups of the macrocycle. Such materials supported on carbon have been shown to be active for oxygen reduction in a fuel cell environment, although activity decreases quickly

* Corresponding author.
E-mail address: ozkan.1@osu.edu (U.S. Ozkan).

0021-9517/$ – see front matter
doi:10.1016/j.jcat.2006.01.022

over time. These materials can be made more stable by subjecting them to high-temperature pyrolysis while on the carbon support before use in the low-temperature reaction. However, it is believed that the active metal center site completely decomposes at higher temperatures, at which point the resulting catalysts become more active and stable in the cathode environment [4]. The configuration of the new active site is as of yet unknown, although researchers have hypothesized sites ranging from metal atoms still stabilized by nitrogen groups [5,17] to sites that contain no metal but are formed catalytically in the presence of metal [10–12,18,19].

More recently, it has been shown that active catalysts can be produced from a wide variety of metal, carbon, and nitrogen starting materials [13,16,17,20–28]. Even simple materials like iron salt, carbon black, and ammonia can be subjected to a heat treatment to produce active ORR catalysts. The nature of the active site is still not well understood, although an active site has been proposed in which Fe is stabilized by pyridinic nitrogen groups on the edge plane of the carbon, similar to a 1,10-phenanthroline molecule [17]. The presence of such a site is based on time of flight secondary ion mass spectrometry (ToF-SIMS) results [17], as well as the fact that the 1,10-phenanthroline molecule is known to adsorb Fe ions in solution. But research has shown that active catalysts can be produced by the heat treatment of carbon supports with no metal doping in the presence of a nitrogen source, although activity is less than that in samples to which Fe was added [26]. In these cases, activity was attributed to metal contamination of the carbon supports, because carbon black inherently contains metal contamination from its preparation.

Some researchers, on the other hand, have hypothesized that Fe may not be part of the active site, but may simply act as a catalyst for the formation of the active site [10–12,18,19,21]. Evidence for such a hypothesis includes the fact that activity can improve after treatment with acid or Cl_2 [21], which removes Fe, and that 70 ppm (the Fe contamination in Vulcan carbon) is a relatively small amount of Fe to contribute significant catalytic activity. Although there is a lack of proposed mechanisms for the ORR in acidic media that include a non-metallic active site, the literature does contain several clues as to how nitrogen could improve the ability of carbon to reduce oxygen. Strelko et al. modeled the electron-donating properties of carbon containing hetero-atoms [29,30] and found that replacing carbon with nitrogen improves the ability of graphite to donate electrons to O_2 or other reactants. In simplified terms, nitrogen can be viewed as an n-type dopant, such that when it replaces carbon in the graphite matrix, the plane will contain an extra electron that is more easily donated. Another possibility is the potential improvement in performance caused by the presence of pyridinic nitrogen species at the edge plane. Montoya et al. modeled the combustion of nitrogen-containing carbon in oxygen [31,32] and found that the formation of a pyridinic–N^+–O^- species is exothermic and a likely intermediate in the combustion of nitrogen-containing carbons to NO. A significant amount of XPS analysis of nitrogen-containing carbons has hypothesized the presence of such a species to explain peaks at a higher oxidation state in the N 1s region [33–35]. It is possible that such a species could be an intermediate for oxygen reduction to water at pyridinic nitrogen sites.

If iron is not part of the active site (or even if it is), it may be acting as a catalyst for the formation of active sites by increasing the number of edge planes exposed. Many electrocatalytic reactions show increased kinetics on carbon edge planes compared with basal planes [36–39]. In fact, even the reduction of oxygen in alkaline solutions has been shown to occur faster on carbon edge planes [36,37]. This increase in activity is attributed to the ability of edge planes to more readily chemisorb oxygen, the same reason that carbon combusts faster from edges and defects [36]. Therefore, if nitrogen were merely playing the role of a dopant, then edge planes would still likely improve activity because of their known increased interaction with oxygen. Conversely, if nitrogen were part of an "active site," then incidentally both of the proposed active sites, pyridinic nitrogen and the 1,10-phenanthroline site, would be found on the carbon edge plane.

Metal particles, such as Fe and Ni, are often used as catalysts for the controlled formation of various forms of carbon nanostructures [40–44]. Different nanostructures inherently have more edges exposed than others, as Fig. 1 illustrates. Structures like onions and tubes (especially longer tubes) have mostly basal planes exposed, whereas carbon fibers with stacked platelet or stacked cup structures have significant edge plane exposure. The conditions used to prepare these structures are strikingly similar to the treatment conditions used to prepare active oxygen reduction catalysts. Various conditions, including temperature, atmosphere, and the metal catalysts used, ultimately control the type of nanostructures that form [40,43]. The role of Fe in the formation of particular nanostructures during the preparation of active ORR catalysts from simple precursors, other than observing the presence of filamentous carbon [21,24,45], has not been thoroughly investigated.

In this work we investigate the role of metal particles in the formation of specific nitrogen-containing carbon nanostructures and their relation to ORR activity. Both Fe and Ni supported by Vulcan carbon were compared with pure Vulcan carbon as a platform for acetonitrile pyrolysis. Several char-

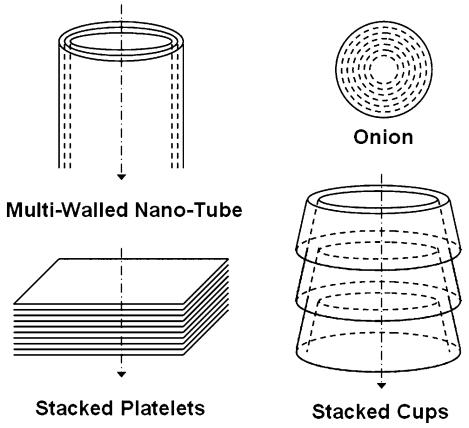

Fig. 1. Schematic drawings of common carbon nanostructures demonstrating plane orientation relative to the central axis and thus the resulting edge plane exposure.

acterization techniques were used to identify the properties of the resulting materials, including BET surface area analysis, BJH pore size distribution (PSD), conductivity testing, transmission electron microscopy (TEM), temperature-programmed oxidation (TPO), thermogravimetric analysis (TGA), X-ray diffraction (XRD), X-ray photoelectron spectroscopy (XPS), and rotating disk electrode (RDE) half-cell testing. In particular, XPS and TEM characterization was used to investigate whether metal particles improve the amount of nanostructures with a significant amount of edge planes exposed and thus a higher amount of pyridinic nitrogen. Characterization results were correlated with oxygen reduction activity determined from RDE half-cell experiments.

2. Experimental

2.1. Catalyst preparation

Commercial Vulcan carbon XC-72 (Cabot, as received) and Vulcan carbon doped with 2 wt% Fe or 2 wt% Ni were used as a support for the high-temperature pyrolysis of acetonitrile to produce active catalysts. In cases where the support was doped with a metal before acetonitrile deposition, the desired amount of metal acetate salt was dissolved in 100 mL of double-distilled H_2O, and then the support was added to the solution while stirring vigorously. The suspension was then sealed and shaken to wet the carbon, which can form a film on the water surface. The sample was then stirred for another 30 min and sonicated for 20 min before drying overnight at 100 °C.

Acetonitrile decomposition, or pyrolysis, was carried out by first adding 2.0 g of support to a quartz calcination boat and sealing it inside a quartz tube furnace. The temperature was then ramped at 10 °C/min up to the treatment temperature under the carrier gas (N_2 unless noted otherwise) flowing at 150 sccm. Once the furnace reached the desired treatment temperature, the room-temperature carrier gas was saturated with acetonitrile ($p_{vap} = 72.8$ mm Hg) using a bubbler before being sent to the furnace. After the treatment was complete (times varied), samples were cooled to room temperature under the carrier gas. In addition, two samples were prepared by decomposition of acetonitrile in the absence of a support for comparison. The same conditions were used, but for the first sample within an empty quartz tube, the treatment time lasted 18 h, and the resulting graphite flakes had to be scraped off the side of the tube walls. The other sample was prepared under identical treatment conditions for 2 h with 200 mg of unsupported Fe(II) acetate in the furnace.

A sample was also prepared within a sealable quartz tube for controlled-atmosphere XPS analysis. As-received Vulcan carbon (100 mg) was used as the platform for the pyrolysis and was placed in a $\frac{1}{4}$-inch-i.d. quartz tube with quartz wool packed on each side. The tube was then placed in an in-house-built horizontal high-temperature tube furnace. Valves were connected to each end of the quartz tube using graphite ferrules. The valves were far enough away from the furnace to prevent their seals from failing. The temperature was then raised to 900 °C at a rate of 10 °C/min under N_2 flow at 50 sccm. At that point, the N_2 was sent through a room-temperature bubbler to saturate the feed with acetonitrile. After 4 h, the flow was switched back to N_2, and the temperature was allowed to cool to 100 °C; then the sample was sealed in the quartz tube by closing the valves and taken to a glove box for XPS analysis preparation.

2.2. BET surface area and pore size distributions

Surface area measurements were made by N_2 physisorption using both a Micromeritics ASAP 2010 and a Micromeritics Accusorb 2100E. The BJH pore size distributions were obtained from the desorption isotherms of N_2 physisorption experiments with the Micromeritics ASAP 2010.

2.3. Conductivity testing

Estimates of the bulk material conductivity were obtained to determine the electrical resistance of the materials in a fuel cell environment. For these measurements, a 1:1 mass ratio of sample to 5 wt% Nafion in a solution of aliphatic alcohols was mixed with an additional 10 mass equivalents of ethanol, and then sonicated for 30 min. (This process mimics the catalyst ink preparation for fuel cell cathode preparation.) Next, the ink was distributed evenly on a copper plate covered with Teflon tape that had a small hole punched through the tape to act as a reservoir for the catalyst ink. Sufficient ink was added to evenly fill the reservoir with catalyst. After the catalyst dried, the plate was clamped to a bare copper plate using a force of approximately 100 psi with only the catalyst making electrical contact between the plates (because the Teflon tape is not conductive). The plates were then connected to a PAR 263A potentiostat, and the voltage was swept from 0 to −0.1 V to determine conductivity. Resistance in the Cu plates was accounted for in the conductivity calculation. Each sample was measured four times; the average standard deviation was ±5% or less for this group of samples.

2.4. TGA

Acetonitrile deposition for catalyst preparation was performed in situ while following weight changes with a Setaram TGA/DSC 111 for selected precursors. The instrument was placed in corrosive gas mode, and approximately 10 mg of support was loaded in a quartz crucible, while an empty quartz crucible used on the reference side of the balance. To study temperature dependence, the temperature was ramped from 20 to 800 °C at a rate of 5 °C/min under a flow of N_2 saturated with acetonitrile at room temperature (50 sccm split between both sides), then held at 800 °C for 2 h before ramping back down to 20 °C. To study weight changes as a function of treatment time, the temperature was ramped from 20 to 800 °C at a rate of 5 °C/min under N_2 flow. At 800 °C, the N_2 was saturated with acetonitrile (at room temperature) before being sent to the sample and reference. After 12 h of treatment, the analysis was stopped.

2.5. TPO

Carbon samples were characterized by TPO using an on-line Shimadzu QP-5050 gas chromatograph–mass spectrometer. In the experiments, 10 mg of sample was placed in a $\frac{1}{4}$-inch-i.d. quartz U-tube between pinches of quartz wool, then flushed with 10% O_2 in He flowing at 30 sccm for 20 min. Next, the temperature was ramped from room temperature to 800 °C, at a rate of 5 °C/min, while flowing the same gas mixture, and the oxides of H, C, and N were measured.

2.6. XRD

XRD patterns were obtained with a Bruker D8 diffractometer using Cu-K_α radiation. Samples were supported by polyethylene holders with a 0.5-mm-deep reservoir for the powder samples. Patterns were recorded between 10° and 90° 2Θ.

2.7. XPS

XPS was carried out with a Kratos Ultra Axis on samples to determine surface composition of the elements present and also to gain insight into the nature of their structures on the surface. For each sample, a survey was performed from 1200 to 0 eV using a Mg anode at 14 kV and a 10 mA current. Next, five sweeps were carried out for each element concurrently, with the C 1s, N 1s, and O 1s region always scanned. Air-sensitive samples were transferred into the instrument using a glove box and a controlled-atmosphere transfer chamber. The estimated water and oxygen concentrations in the glove box was <5 ppm, and each sample was exposed to this environment for <20 min.

2.8. TEM

TEM was performed with Phillips CM300 Ultra-Twin FEG and Phillips Tecnai TF20 instruments. Before being placed on the support, the samples were dispersed in excess ethanol by sonicating for 30 min. Lacey-formvar carbon supported by a 200-mesh copper grid was used as a support.

2.9. RDE half-cell activity testing

The activity of all samples for the ORR was gauged with cyclic voltammetry (CV) experiments using a PAR 263A potentiostat/galvanostat with a 616 RDE setup. Approximately 10 μL of catalyst ink (prepared for conductivity testing) was dispensed on the glassy carbon RDE so as to completely cover the glassy carbon current collector but not the Teflon, and then allowed to dry. For the testing, a 0.5 M solution of H_2SO_4 was used as the electrolyte. The solution was purged with pure O_2 before performing an initial test sweep from 1.2 to 0 V (vs. NHE) at 10 mV/s to remove gaseous O_2 from the catalyst pores and allow the pores to fill with solution. Next, the solution was sparged with argon for 30 min to remove O_2 from the electrolyte. Then five consecutive CVs were run from 0.0 to 1.2 to 0.0 V (vs. NHE) at 50 mV/s, to confirm the absence of oxygen and to obtain a steady current by cleaning reducible and oxidizible contaminants off of the electrode. Next, a baseline was obtained by sweeping from 1.2 to 0.0 to 1.2 V (vs. NHE) at 10 mV/s in the argon sparged solution at a 0-rpm rotation rate. Finally, the solution was saturated with O_2 until consecutive CVs matched (0.0 to 1.2 to 0.0 V at 50 mV/s), and slow CVs (10 mV/s) were then taken at rotations from 0 to 2000 rpm in 250-rpm increments in an alternating order converging on 1000 rpm (0, 2000, 250, 1750, etc.). After testing, the RDE was polished with an alumina and water slurry. The electrolyte was changed after every sample. The voltage of the peak oxygen reduction current at 0 rpm is reported as a measure of activity. In addition, Koutecky–Levich plots of $1/I$ (A^{-1}) versus $1/\omega^{1/2}$ ($s^{1/2}\,rev^{-1/2}$) were constructed from data to obtain the electron coefficient n and the kinetic current, as described in the next section.

3. Results and discussion

3.1. Catalyst preparation and physical characterization

The growth of carbon nanofibers from a carbon source has been well studied using Fe-, Co-, and Ni-based catalysts [40,43,46,47]. Depending on the catalyst, fiber growth usually starts at around 600 °C, the temperature at which carbon can adsorb on the metal surface, diffuse through the metal particle, and deposit out the opposing side of the particle in the form of elemental carbon [40]. Some researchers have prepared nitrogen-containing carbon fibers, although the presence of nitrogen often requires higher temperatures for fiber growth. These fibers can be grown from acetonitrile or other vapors using Ni- and Co-based catalysts [46,47]. Consequently, researchers have also prepared active ORR catalysts for PEM fuel cell cathodes from the pyrolysis of acetonitrile vapors (and other nitrogen/carbon mixtures) in the presence of Fe particles [21,24,45]. Fibers were observed in these catalysts among other nanostructures, although the nanostructures of the fibers were not studied, and activity could not be attributed to the fibers themselves. A loading of 2 wt% Fe on the support was found to be the optimal loading in these studies. However, because active ORR catalysts have been reported only for nitrogen and carbon decomposed in the presence of Fe, it was decided to compare catalysts made in the presence of both Ni and Fe, because Ni often catalyzes fiber growth.

Determining the temperature needed to initiate carbon growth was the first step in catalyst preparation. TGA experiments were run to see what temperature carbon deposition takes off on the various supports as the temperature is increased. Table 1 shows the temperature at which sample weight began to increase in the presence of acetonitrile-saturated N_2. The

Table 1
Take-off temperatures of acetonitrile deposition on various supports

Sample	T (°C)
Vulcan carbon (VC)	610
2% Fe/VC	560
2% Ni/VC	532

presence of 2 wt% Fe or Ni on the support decreased the temperature at which fiber growth commenced, with the Ni sample taking off at the lowest temperature. Interestingly, researchers studying Fe/N/C chars as catalysts for the ORR have observed that pyrolysis temperatures between 600 and 900 °C (the same temperature range in which fiber growth can occur) yield active catalysts [16].

The subsequent TGA experiments sought to determine an acceptable treatment time for catalyst preparation. In these experiments the temperature was raised to 800 °C and kept there for 12 h to observe the weight increase trend. Fig. 2 shows the comparison of Fe-doped Vulcan carbon to pure Vulcan carbon. Both samples continued to increase in weight through the duration of the treatment; however, the metal-doped sample gained weight much more rapidly than the nonmetal sample.

Based on these trends, a series of catalysts were prepared using the supports of interest with treatment temperatures varying between 600 and 900 °C and treatment times varying from 20 min to 12 h. For all of these samples, some initial properties were measured, including weight gain during treatment, BET surface area, nitrogen content, and ORR activity. Weight gain during the treatment is defined as the difference between the weight of the sample before and after pyrolysis, divided by the weight before (an identical definition to the value used for the y-axis of the TGA plots). The percentage of the surface composed of nitrogen atoms was determined from XPS analysis, as discussed in more detail in the next section. A quick and easy estimate of the activity of these samples for the ORR was also performed using a RDE half-cell setup in which the catalyst was placed in a 0.5 M H_2SO_4 electrolyte saturated at room temperature with O_2, and the voltage was cycled while recording the current. A peak in the current is observed as the O_2 in the vicinity of the catalyst is used up. This peak occurs at a voltage closer to the theoretical ORR voltage of 1.2 versus NHE for more active catalysts. This technique is commonly used by ORR catalyst researchers for gauging activity, and additional kinetic information can be obtained from these experiments by rotating the sample, as explained in the section on activity testing. At this point, it is important only to note that more active catalysts will reduce oxygen at a higher voltage and thus have a higher ORR peak potential. For reference, a 20 wt% Pt/Vulcan carbon commercial catalyst (Electrochem, EC20PTC), had an ORR peak potential of 750 mV versus NHE in our measurements.

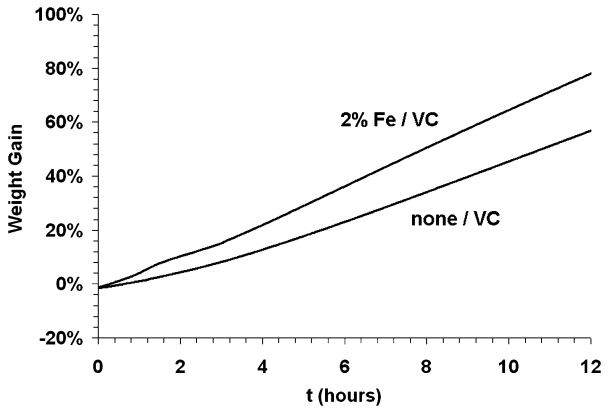

Fig. 2. Gravimetric analysis during pyrolysis of acetonitrile at 800 °C comparing Vulcan carbon and 2% Fe/VC supports.

The properties of the initial series of catalysts are given in Table 2. Untreated Vulcan carbon, which contains no nitrogen, is a poor catalyst for the ORR. However, treating the sample with acetonitrile results in weight increase (dependent on time), nitrogen uptake, and improved catalytic activity, with a 2-h treatment giving the most active catalyst. The same trend holds true if 2 wt% Fe is present on the carbon before the treatment. In the case of the Fe-containing samples, the weight gains are much higher, the final surface areas are higher, and the activities are higher. The Fe samples treated at lower temperatures were not as active as the samples treated at 900 °C, possibly because despite having similar weight gains and surface area, these samples have a lower nitrogen content. Treatments were not carried out above 900 °C, but other researchers have reported that treatment at 1000 °C yielded a catalyst with lower nitrogen content and lower activity than treatment at 900 °C [4,16]. Nickel is also a common catalyst for carbon fiber growth, but treatment of 2 wt% Ni on Vulcan carbon did not

Table 2
Properties of Vulcan carbon-based catalysts treated in acetonitrile

Support	Treatment T (°C)	Treatment time	Weight increase (%)	BET S.A. (m^2/g)	N composition from XPS (%)	ORR current peak (mV)
VC	As received	None	–	230	0.0	30
VC	900	12 h	101.8	26	8.2	140
VC	900	2 h	20.2	90	3.6	240
VC	900	20 min	3.3	158	1.2	180
2% Fe/VC	900	12 h	147.5	39	8.6	355
2% Fe/VC	900	2 h	39.0	127	3.5	555
2% Fe/VC	900	20 min	10.0	162	1.5	550
2% Fe/VC	800	2 h	22.6	154	0.7	430
2% Fe/VC	700	12 h	14.1	134	0.8	315
2% Fe/VC	700	2 h	2.0	200	0.7	460
2% Ni/VC	900	2 h	22.2	90	4.2	175
2% Ni/VC	800	2 h	8.2	119	1.1	160
2% Ni/VC	700	12 h	9.8	134	0.6	145
2% Ni/VC	700	2 h	1.8	203	0.7	270
2% Ni/VC	600	12 h	1.4	200	<0.6	175

give the favorable properties and activities seen in the Fe-containing samples. Other researchers have hypothesized that Fe is part of the active site for the ORR, and that samples supported by Vulcan carbon that demonstrate some activity are active because of the inherent Fe contamination (70 ppm) in the commercial carbon. But this initial characterization indicates there Fe may play an additional role, considering the higher weight gains and surface areas of the Fe-doped samples. Fig. 3 clearly demonstrates that for treatment at 900 °C, the Fe-based samples maintained higher surface areas despite achieving higher weight gains.

Before examining more physical properties, we note that interesting results occur when samples are prepared without a support or are heated in the absence of acetonitrile. Table 3 shows the properties of such samples. When Vulcan carbon is treated in pure N_2 rather than acetonitrile-saturated N_2, the activity for oxygen reduction does not improve. If Fe is present on the support before the N_2 treatment, then the activity improvement is very small versus that of plain carbon, demonstrating that acetonitrile is necessary for significant catalytic improvement. If acetonitrile is decomposed in the absence of a high-surface area support, then the final product has very low surface area and little activity for oxygen reduction. When Fe acetate alone is treated in the presence of acetonitrile, there is a significant weight increase, but the final surface area and activity are low. These results, together with the initial series of catalysts, support the hypothesis that active catalysts need to be a carbon material with high surface area and contain nitrogen but need not necessarily contain iron to have higher activity, unless the 70-ppm Fe contamination is sufficient to contribute activity.

Pore size distribution analysis of some selected samples showed a unique feature for samples in which Fe was present during the decomposition of acetonitrile (Figs. 4a–c). After

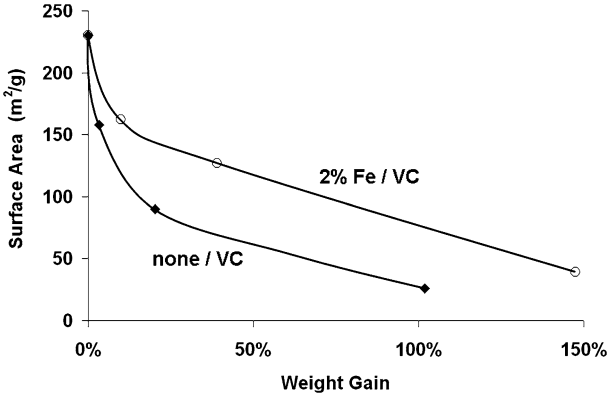

Fig. 3. Comparison of surface areas as a function of weight gain for Vulcan carbon and 2% Fe/VC samples treated at 900 °C in acetonitrile for various times.

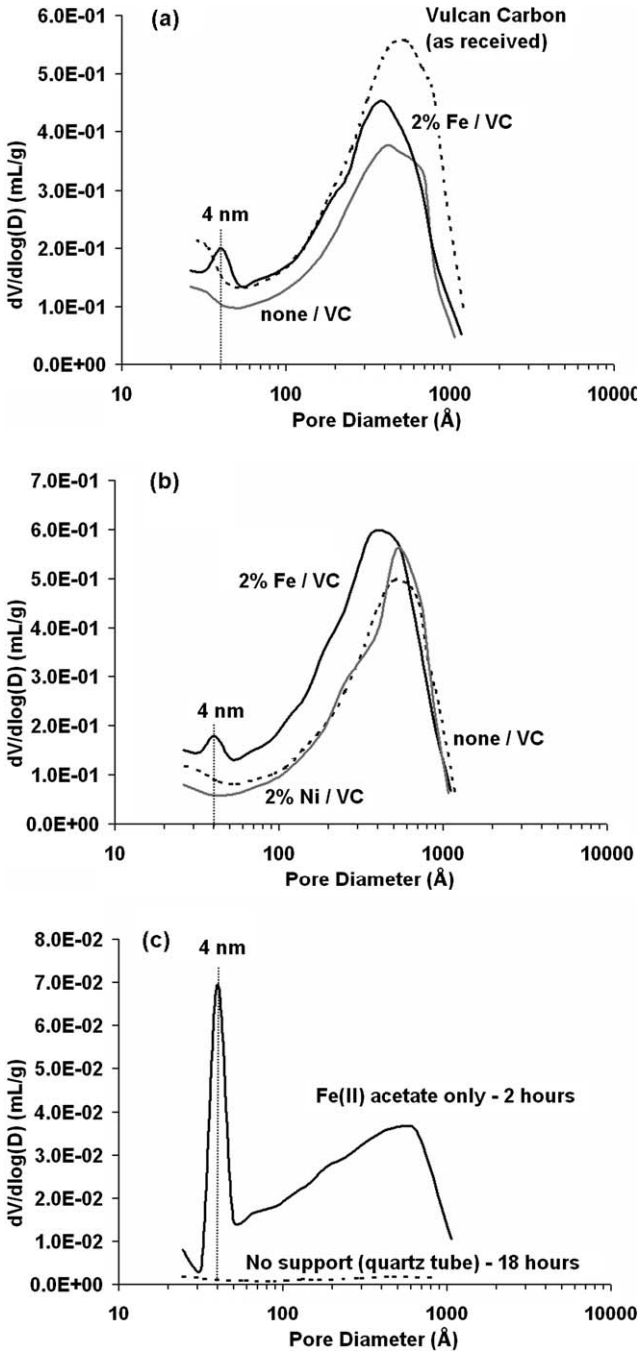

Fig. 4. Comparison of pore size distributions after pyrolysis of acetonitrile at 900°C for (a) samples treated 20 min with untreated Vulcan carbon shown for comparison, (b) samples treated 2 h, and (c) treated unsupported low surface area samples.

Table 3
Properties of samples prepared using various supports and atmospheres at 900 °C

Support	Atmosphere	Weight increase (%)	BET S.A. (m^2/g)	N composition from XPS (%)	ORR current peak (mV)
VC	N_2 only	−0.6	228	0.0	10
2% Fe/VC	N_2 only	−2.1	234	0.0	165
None	CH_3CN	Undefined	1.5	3.3	5
Fe acetate	CH_3CN	43.2	9	1.5	25

20 min of treatment, both Fe-doped and nondoped samples lost some pore volume; however, the Fe-doped sample had a higher distribution of smaller pores and a peak distribution at 4 nm (Fig. 4a). The same trends held after 2 h of treatment, as shown in Fig. 4b. This feature at 4 nm likely arises from nanofiber growth from Fe particles. Apparently, such fiber growth does not occur in Ni-doped or nondoped Vulcan carbon samples. Interestingly, Fig. 4c demonstrates that fiber growth likely occurs on unsupported Fe as well, because unsupported Fe acetate treated in acetonitrile at 900 °C resulted in a sharp peak at 4 nm. In contrast, the graphitic flakes formed from acetonitrile pyrolysis in an empty furnace had very little pore volume and no discernible features in the pore diameter distribution. The peak at 4 nm may not necessarily be due to pores exactly at 4 nm. In other nanoporous materials, it has been documented that a N_2 tensile strength effect can cause an apparent peak in the BJH desorption PSD at around 4 nm [48]. However, the PSD analysis clearly demonstrates there is something different about the Fe-doped samples on the nanoscale after the pyrolysis of acetonitrile.

Further physical characterization provides some insight into the nature of the carbon forming during the treatments. XRD patterns for a series of carbon-derived samples are shown in Fig. 5. Amorphous Vulcan carbon has a very broad characteristic (002) peak corresponding to a d-spacing of 0.363 nm. The nitrogen-containing graphite flakes formed from the decomposition of acetonitrile without a support have a (002) peak corresponding to a d-spacing of 0.338 nm. The peaks for all samples analyzed were very broad, indicative of small crystallite size (<10 nm) or lack of long-range order. The samples that underwent higher weight gains were those that displayed a shift in the C (002) peak from that of Vulcan carbon to the peak consistent with nitrogen containing graphite flakes formed in the absence of a high-surface area support. This finding indicates no correlation between this peak and activity (because there are apparently other important properties for activity); however, it does demonstrate how 2% Fe/Vulcan carbon treated for only 2 h in acetonitrile (the best catalyst studied thus far) led to a shift in the (002) peak unlike the other samples treated for 2 h, and that a new type of carbon formed during the treatments.

TPO experiments were carried out to check whether the results correlated with the activity of samples for oxygen reduction. It is conceivable that samples that are more active for the ORR will activate oxygen at lower temperatures and thus combust more quickly. Comparing as-received Vulcan carbon and acetonitrile char (shown in Fig. 6) reveals that the nitrogen-containing carbon combusts at a much lower temperature. This is somewhat surprising, because the acetonitrile char has a very low surface area, which should make it combust more slowly. Both carbon samples combust to form both CO (28 amu) and CO_2 (44 amu and a small 28 amu contribution); however, only CO is shown in the figure. The patterns were similar for CO_2 and CO except when the combustion rate was high, at which point CO_2 formation reached a plateau (likely from a drop in O_2 concentration) and the CO abundance formed a smooth peak. For both samples, CO_2 intensity was slightly higher than CO intensity. The combustion of Vulcan carbon did not lead to the formation of any nitrogen oxides, whereas some NO (30 amu) but virtually no NO_2 (46 amu) was formed during the combustion of the acetonitrile char. Interestingly, although nitrogen oxide was released simultaneously with the carbon oxides, most of the NO was produced toward the final stage of char combustion.

Fig. 7 shows that the presence of a metal decreases the combustion temperature and causes a sharp spike in the amount of CO and CO_2 released, with Fe decreasing the combustion starting temperature more than Ni. Again, the patterns were identical for 44 and 28 amu, with 44 amu being about 50% more intense. The fragmentation of pure CO_2 would predict 44 amu to have 10 times the intensity of 28 amu if only CO_2 were formed; thus, obviously CO was forming together with CO_2. Nitrogen oxides peaks (not shown) accompanied the much larger car-

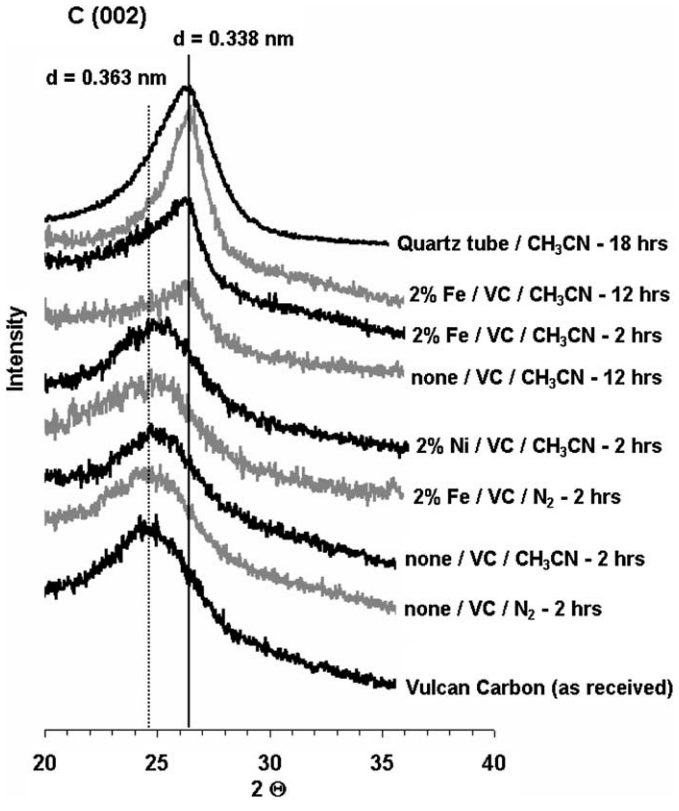

Fig. 5. X-Ray diffraction patterns of various samples subjected to treatments of acetonitrile or nitrogen at 900 °C for various time periods.

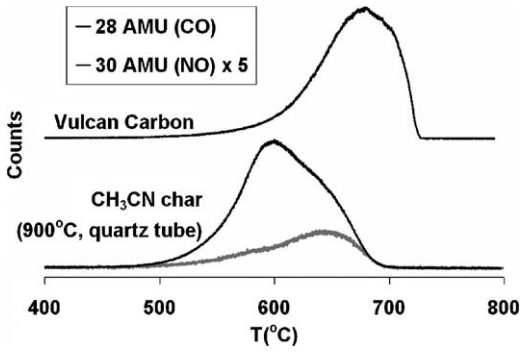

Fig. 6. Temperature-programmed oxidation profiles of untreated Vulcan carbon and 900 °C treated acetonitrile char.

bon oxide peaks with no major differences with respect to the carbon oxide peaks other than intensity. The Vulcan carbon sample treated in acetonitrile without metal addition combusted at a higher temperature than the metal-containing samples and even acetonitrile char. During preparation, this sample received only a 20% weight gain from the acetonitrile decomposition; thus, the sample may be mostly Vulcan carbon. The other samples may also consist mostly of Vulcan carbon, but the metal is likely acting as a catalyst for combustion, making the samples burn at much lower temperatures than the pure carbon would. To really characterize carbon fibers with TPO, the metal must be removed by extensive washing to prevent any effect on the combustion profile [49]. Because of this catalytic combustion effect of the metal, TPO has a limited ability to characterize the metal-containing samples, but even acid-washed samples will contain metal particles encased in carbon that can affect TPO profiles.

Another very important physical property for fuel cell electrode materials is electrical conductivity. Table 4 reports the conductivities of the samples measured in a typical fuel cell environment. All of the carbon-based samples have slightly higher conductivities than Vulcan carbon. This better conductivity can be attributed to either increased particle size or loss of oxide surface species during treatment. Both of these effects are expected to occur during the treatment and are known to typically increase electrical conductivity in carbon materials [36].

3.2. XPS and TEM

Whereas the foregoing characterization techniques provided results on the physical properties of the samples, the effects of the preparation parameters on nanostructure and surface species can be better characterized by TEM and XPS, respectively. Nitrogen-containing carbons have been studied extensively, particularly with XPS, for coal and Li ion battery electrode applications. Pels et al. performed a detailed XPS analysis of the transformation of carbon and nitrogen model compounds into nitrogen-containing graphite during high-temperature pyrolysis [33] and reported that nitrogen functional groups in carbon decompose at higher temperatures to form two species, quarternary nitrogen and pyridinic nitrogen. Quarternary nitrogen can be described as "graphitic nitrogen," in which nitrogen is within a graphite plane and bonded to three carbon atoms. This type of nitrogen is known to have a characteristic N 1s peak in the XPS spectra at around 401.3 ± 0.3 eV. Pyridinic nitrogen exists on the edge of graphite planes, where it is bonded to two carbon atoms, donates one p electron to the aromatic π-system, and has a resulting N 1s binding energy near 398.6 ± 0.3 eV. Therefore, XPS can be used to quantify these species based on differences in the N 1s spectra.

Although the two previously mentioned nitrogen species are the most stable in carbon treated at high temperatures (>600 °C), some additional nitrogen functional groups are possible in carbon. Pyrrolic nitrogen is often assigned to peaks at 400.5 ± 0.3 eV. Pyridone (pyridinic-N next to an OH group) has a similar assignment, and the two are considered indistinguishable [33]. Both of these species have been shown to decompose at temperatures above 600 °C to pyridinic-N and quarternary-N [33]. A nitrogen species has also been reported in pyrolyzed samples with a high binding energy (402–405 eV), typical of oxidized nitrogen. Several authors have termed this feature a pyridinic–N^+–O^- species that forms after the sample is exposed to air [33–35]. The species discussed thus far are depicted in Fig. 8. Computer simulations have shown that the pyridinic–N^+–O^- species can form during the combustion of nitrogen-containing carbon with oxygen [32]. However, assignment of a pyridinic–N^+–O^- peak cannot be made with a high level of certainty. Fig. 9 compares the N 1s region for Vulcan carbon after treatment with acetonitrile at 900 °C for 2 h. The O 1s spectra could not contribute any useful information in this regard because of the low oxygen concentrations on the surface

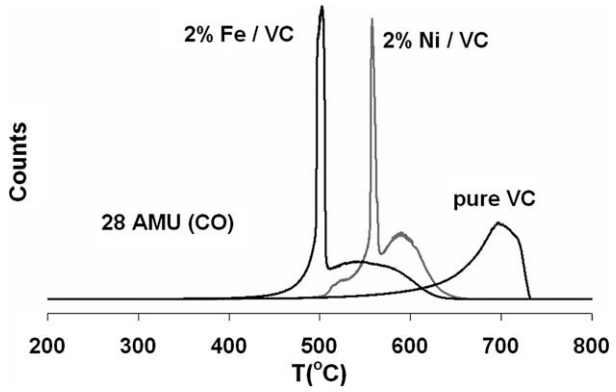

Fig. 7. Temperature-programmed oxidation profiles of doped and undoped Vulcan carbon supported samples treated at 900 °C in acetonitrile atmosphere.

Table 4
Conductivities of various samples

Metal/support	Treatment	Conductivity (S/m)
None/VC	As received	71
20% Pt/VC	Commercial	47
None/VC	CH_3CN for 2 h, 900 °C	111
None/VC	CH_3CN for 12 h, 900 °C	165
2% Fe/VC	CH_3CN for 2 h, 900 °C	117
2% Fe/VC	CH_3CN for 12 h, 900 °C	98
2% Ni/VC	CH_3CN for 2 h, 900 °C	119

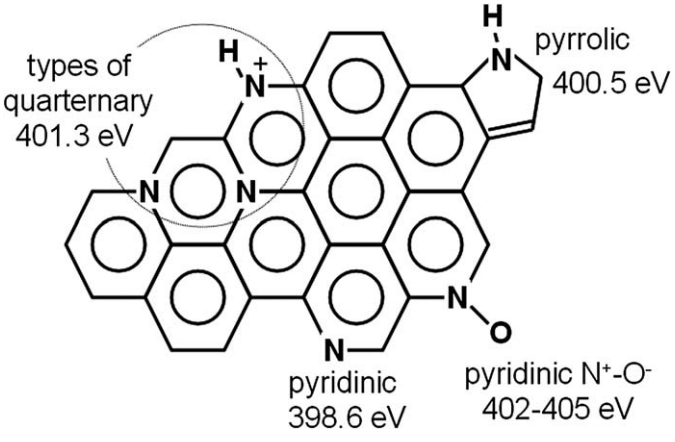

Fig. 8. Nitrogen species commonly reported in post pyrolyzed nitrogen-containing carbon.

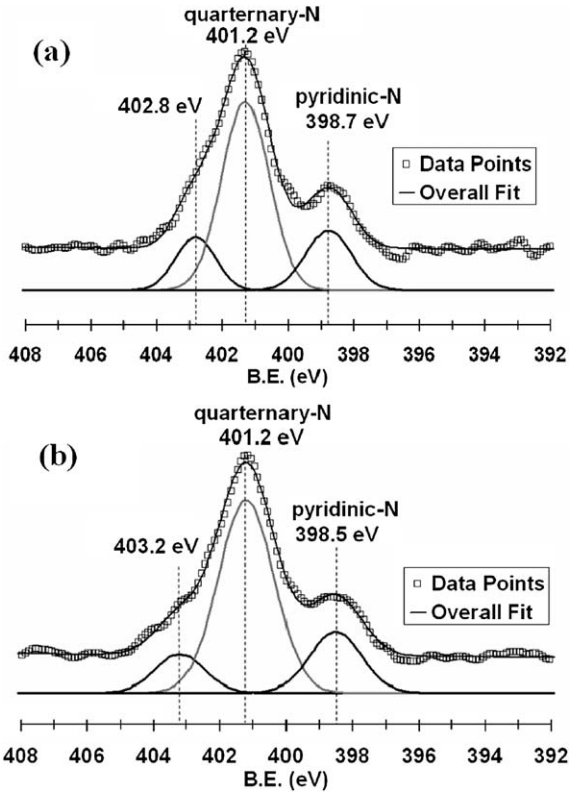

Fig. 9. Comparison of the XPS spectra of the N 1s region for Vulcan carbon treated 2 h at 900 °C with acetonitrile: (a) sample exposed to atmosphere; (b) sample transferred to XPS via a controlled atmosphere transfer chamber.

of the samples (<2%) and the wide variety of possible oxygen species on the surface of carbon, thus further reducing the confidence in any deconvolution in this region.

Alternative assignments to the high-binding energy shoulder in the N 1s region may be related to the interaction of graphitic nitrogen with other nitrogen atoms or to differences in the binding energy of graphitic nitrogen, depending on its position in the graphite plane. For instance, it has been documented that the presence of nitrogen in graphite stretches the C 1s peak to higher values [22]; Fig. 10 shows an example of this phenomenon. It is possible that because some carbon atoms are closer to a nitrogen atom in the graphite matrix than others, some carbon will inherently have a higher C 1s binding energy. The C 1s peak has been shown to grow wider as more nitrogen is added to graphite [22]. A similar phenomenon may occur in the N 1s spectra. Some nitrogen atoms will be closer to one another and thus have higher binding energy. Alternatively, Casanovas et al. developed a hypothesis to explain this shoulder based on modeling of the binding energy of various nitrogen species present in graphite layers [50]. These authors predicted pyridinic-N and pyrrolic-N to have N 1s binding energies of 399.0 eV and 400.3 eV, respectively, similar to the assignments proposed by Pels et al. [33]. However, their calculations revealed that the "graphitic nitrogen" (quarternary-N) can have a binding energy ranging between 401 and 403 eV, even in the absence of oxidized nitrogen, depending on its location in the carbon plane. Because the cause of the higher-binding energy N 1s shoulder is not obvious, this area of the deconvolution was not assigned.

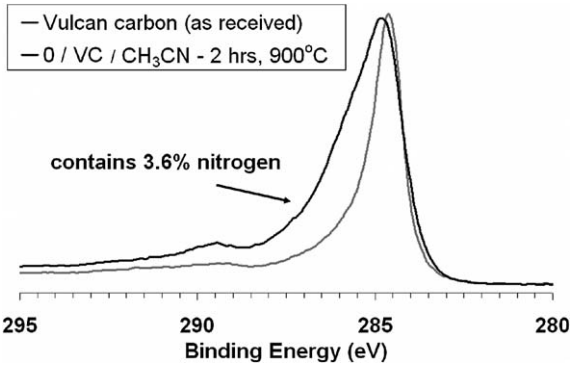

Fig. 10. XPS spectra of the C 1s regions demonstrating the widening of the C 1s peak in a sample containing nitrogen.

In addition, contributions to the N 1s spectra from pyrrolic nitrogen (or pyridone) were ignored for the samples treated at 900 °C, because such species are not thought to be stable at this temperature [33], and during deconvolution they appeared to contribute only minimally, if at all. However, samples treated for shorter times and at lower temperatures were difficult to deconvolute in the N 1s spectra, because the nitrogen content was typically lower and perhaps because pyrrolic nitrogen was more abundant. Consequently, only samples treated at 900 °C for 2 h or longer are compared in this work, and for the purposes of this study, the ratio of quarternary to pyridinic nitrogen is of the greatest importance, because this will give some indication to the extent of edge plane exposure and the corresponding nanostructure.

XPS analysis revealed a correlation between the amount of pyridinic nitrogen and ORR activity. The best carbon-supported sample composed of 2% Fe/Vulcan carbon had a higher proportion of pyridinic-N compared with the other samples, as shown in Figs. 11a–c and in Table 5. If the 2% Fe sample was treated for 12 h, then the activity decrease along with the abundance of pyridinic nitrogen, as shown in Fig. 11c. The acetonitrile char and Vulcan carbon treated for 12 h (not shown) have nearly identical N 1s spectra to the Vulcan carbon sample treated for 2 h with respect to peak ratios. It should be noted that the higher-binding energy shoulder does not correlate with the size of the pyridinic nitrogen peak. In addition to the controlled atmosphere tests mentioned earlier, this is further evidence that the Cassanovas assignment of this peak as graphitic nitrogen is a more likely possibility. The spectra of the samples treated at lower temperatures and shorter times were more difficult to deconvolute reliably because of their lower nitrogen content and therefore are not shown.

At this point, it is important to note that pyridinic-N is not being definitively proposed as the active site for the ORR. Based on the data presented thus far and the previous work of others, it seems reasonable to assert that the active site for the ORR is on the edge plane of the nitrogen-containing graphite. Therefore, the more active samples may contain more pyridinic nitrogen only because these samples have a higher proportion of edge planes exposed, not because pyridinic-N itself is the source of activity. Therefore, TEM imaging was carried out to investigate the nanostructure of the carbon samples, because

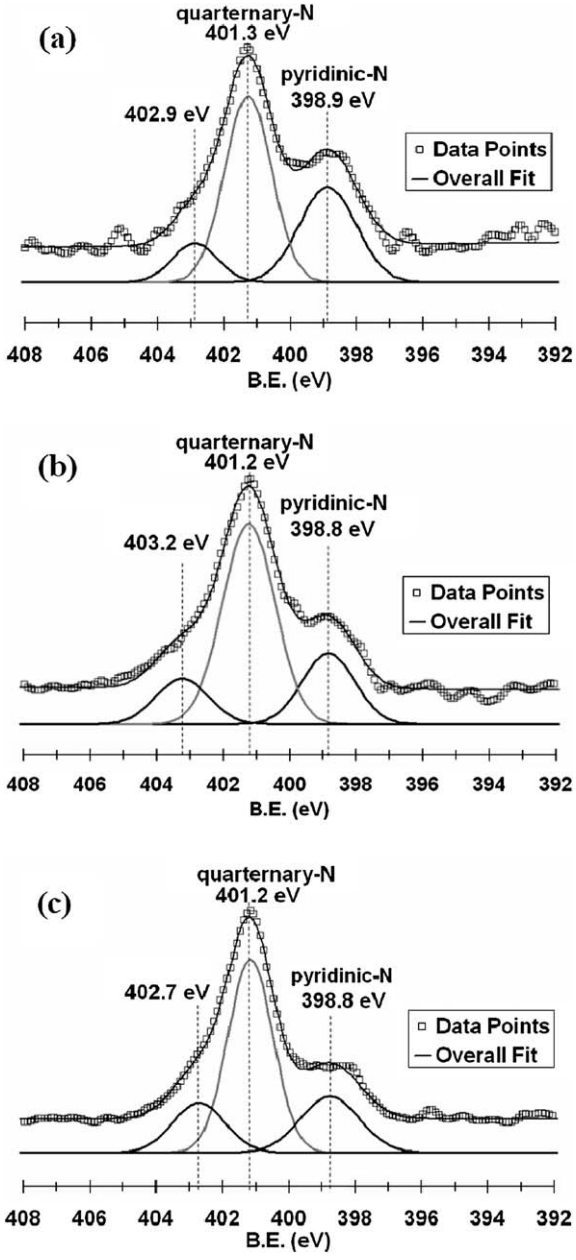

Fig. 11. N 1s spectra of doped Vulcan carbon samples treated at 900 °C in acetonitrile: (a) 2% Fe/VC treated for 2 h; (b) 2% Ni/VC treated for 2 h; (c) 2% Fe/VC treated for 12 h.

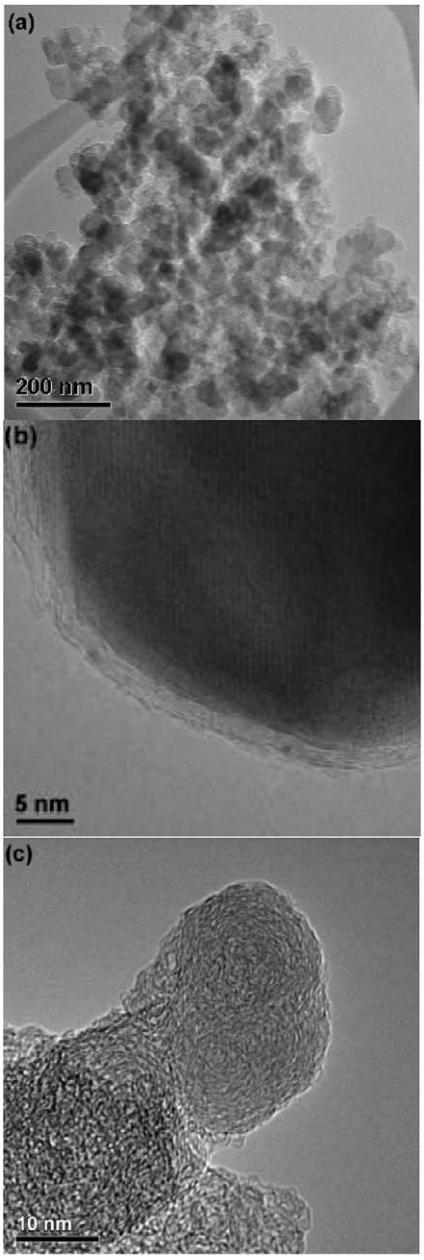

Fig. 12. TEM images of samples treated in acetonitrile vapor at 900 °C for 2 h: (a) 2% Ni/VC; (b) encased Ni particle from 2% Ni/VC; and (c) Vulcan carbon.

high-resolution TEM is useful for directly observing the orientation of graphite planes within nanostructures.

TEM samples were obtained for some selected samples to check for a correlation between the trends seen in XPS and the nanostructure of the carbon. Imaging of the Vulcan carbon samples and the 2% Ni/Vulcan carbon sample revealed no nanostructures within the samples other than weakly graphitic spheres of carbon and Ni particles encased in carbon. Fig. 12a shows a lower magnification of 2% Ni/Vulcan carbon after treatment in acetonitrile at 900 °C, showing an absence of structures other than a mixture of spherical carbon and Ni particles. Fig. 12b shows a high-resolution image of a typical Ni particle covered with several layers of carbon for the same Ni/Vulcan carbon sample. No ordered structures are apparent in the Vulcan carbon sample; only particles similar to the ones depicted in Fig. 12c can be observed.

In contrast, adding Fe to the Vulcan carbon resulted in nanostructures resembling tubes of various diameters. Fig. 13a shows a lower-resolution image of a mixture of carbon fibers in the treated 2% Fe/Vulcan carbon sample. Some of the fibers were typical multiwalled nanotubes, but most had a hollow stacked-cup structure (Fig. 13b). This type of structure has carbon graphite planes that terminate at the outside of the tube, as shown in Fig. 1. The core of this type of structure is electron-transparent and likely hollow or possibly filled with amorphous carbon. The cores of the observed fibers were on the order of 3–10 nm in diameter, possibly accounting for the peak in

Table 5
Overview of the XPS N 1s regions analysis

Sample	Pyridinic-N		Quarternary-N		Shoulder		Note
	B.E. (eV)	N (%)	B.E. (eV)	N (%)	B.E. (eV)	N (%)	
0/VC/CH_3CN 2 h	398.7	19	401.2	65	402.8	16	See Fig. 9a
0/VC/CH_3CN 2 h (cont. atm)	398.5	21	401.2	68	403.2	12	See Fig. 9b
0/VC/CH_3CN 12 h	398.6	23	401.1	63	402.8	14	Not shown
Fe/VC/CH_3CN 2 h	398.9	34	401.3	55	402.9	11	Fig. 11a
Fe/VC/CH_3CN 12 h	398.8	21	401.2	60	402.7	19	Fig. 11c
Ni/VC/CH_3CN 2 h	398.8	22	401.2	63	403.2	15	Fig. 11b
CH_3CN char	398.7	23	401.1	62	402.8	15	Not shown

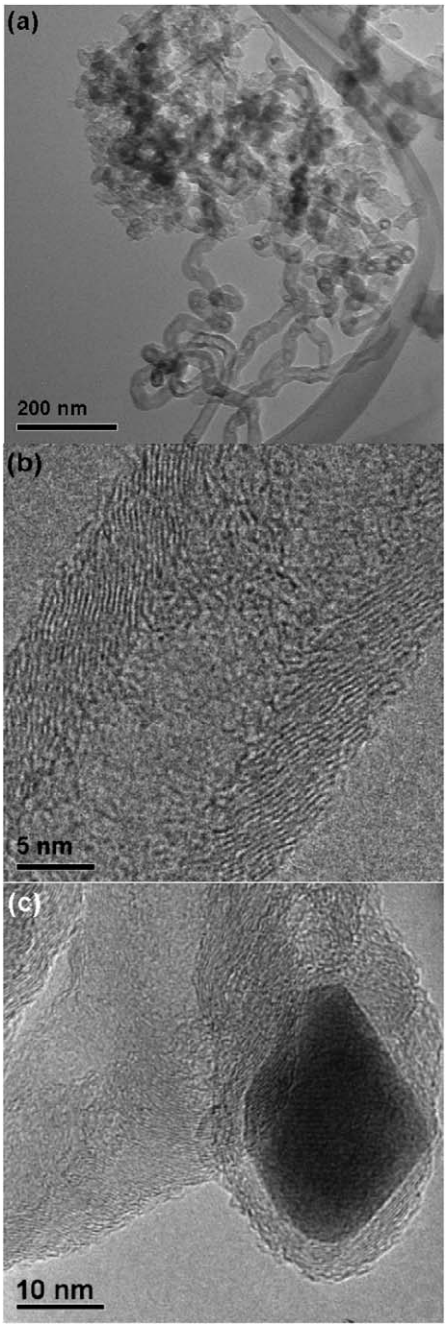

Fig. 13. TEM images of 2% Fe/VC treated in acetonitrile vapor at 900 °C for 2 h: (a) collection of carbon fibers; (b) orientation of carbon planes within a fiber; and (c) encased Fe particle.

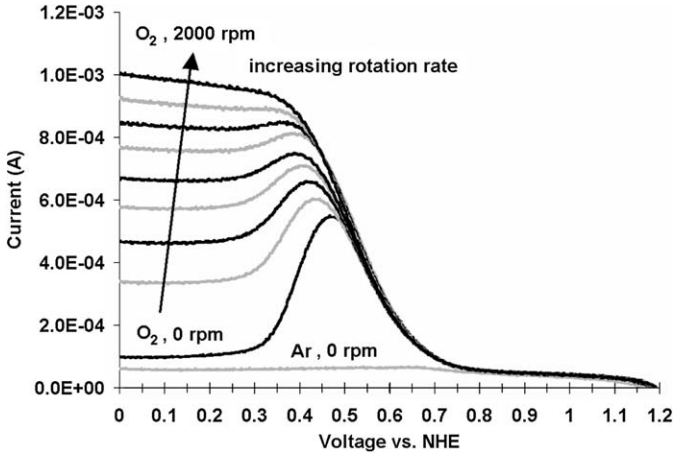

Fig. 14. RDE half cell experimental results for 2% Fe/VC treated for 2 h at 900 °C in acetonitrile.

pore diameter distributions for Fe-containing samples reported in the previous section. As a result of the terminating planes, such a structure will have a large amount of edge exposure, explaining the differences in the quarternary (graphitic nitrogen) to pyridinic (on the edge plane) nitrogen ratio seen in XPS. These structures obviously formed from the metal particles, which were about the same diameter and often encased in the end of the fiber, as shown in Fig. 13c. TEM revealed no amorphous carbon on the fiber surfaces, as is often the case in carbon nanofiber preparation. Overall, the nanostructures and carbon plane alignment seen in this series of samples appear to correlate well with the XPS and activity results.

3.3. Activity testing

More significant information besides relative activity of the samples can be obtained from a RDE half-cell setup. For instance, it is important to know the selectivity of the reduction reaction to water versus hydrogen peroxide. The RDE half-cell setup, in which the catalyst is placed in an oxygen-saturated electrolyte, acts as a model for a fuel cell environment. The electrolyte (0.5 M H_2SO_4) provides protons to the reaction at the cathode similar to a Nafion membrane transporting incoming protons from the anode to the cathode in an actual PEM fuel cell. Oxygen within the solution diffuses to the surface of the electrode and reacts to form water, consuming electrons and producing a measurable current. The potentiostat not only measures the current, but also controls the voltage in the cathode,

thereby giving a measure of the voltage at which the reduction current increases. A smaller voltage drop from the theoretical voltage for the ORR corresponds to a better catalyst. By rotating the electrode at different rates, the mass transfer effects of oxygen diffusion through the solution can be accounted for, and the pure kinetic current can be calculated, giving a true measure of catalytic performance at specific voltages. In addition, if the surface area of the cathode is known, then the number of electrons transferred per mole of oxygen reacting ($n = 4$ for complete reduction to water) can be calculated, providing a measure of selectivity.

The half-cell current/voltage curves for 2% Fe/Vulcan carbon treated 2 h at 900 °C are shown in Fig. 14. The peak in the current (used to gauge relative activity) comes about as oxygen within the vicinity and pores of the sample reacts, and the current then becomes limited by the diffusion of oxygen through the solution to the catalyst surface. As the rotation rate of the electrode increases, the mass transfer of oxygen to the sample increases, thus increasing the mass transfer-limited current. When the current becomes completely mass transfer-limited, it should level out to be parallel with the baseline taken in argon, and not be dependent on voltage. The slight upward slope with voltage observed in our data has been observed by other researchers as well and is perhaps caused by a distribution of active sites in the catalyst [10,51].

Koutecky–Levich plots can be constructed from the RDE data to determine the kinetic current and the number of electrons being transferred. First, the reaction order with respect to O_2 must be verified using the following relationship [10]:

$$\log(I) = \log(I_{\text{kin}}) + p\log(1 - I/I_{\text{l}}),$$

where I is the reduction current, I_{kin} is the kinetically controlled current, p is the reaction order, and I_{l} is the limiting current taken at $V = 0$ when the current levels out. A plot of $\log(I)$ versus $\log(1 - I/I_{\text{l}})$ made using data from a specific voltage had a slope of approximately unity for all samples tested, as long as the current had leveled out at that voltage. Gupta et al. confirmed that the reaction order was 1 with respect to O_2 over pyrolyzed Fe-macrocycle samples using the same technique [10].

Therefore, assuming that the reaction order is 1 for the catalyst at hand, the Koutecky–Levich equation can be applied as a model for the reduction current,

$$1/I = 1/I_{\text{kin}} + 1/I_{\text{l,c}} \quad \text{(Koutecky–Levich equation [2])}.$$

The kinetic current is proportional to the rate of the reaction, which increases exponentially with overpotential [2]. Once the kinetics take off, mass transfer of oxygen in the solution limits the current. The mass transfer-controlled current can be solved from the steady-state convective-diffusion equation written in cylindrical coordinates, and the current is equal to

$$I_{\text{l,c}} = \beta^* \omega^{1/2} \quad \text{(Levich equation [2])},$$
$$\beta = 0.62nFAD_0^{2/3}v^{-1/6}C_0,$$

where n is the number of electrons transferred per reaction, F is Faraday's constant, A is the geometric electrode surface area (as discussed), D_0 is the diffusion coefficient of oxygen through the electrolyte, v is the kinematic viscosity of the electrolyte, C_0 is the bulk concentration of oxygen in the electrolyte, and ω is the rotation rate of the RDE. All of these parameters are constant over the voltage range with the possible exception of n, so both n and I_{kin} can be determined at a particular voltage by plotting I^{-1} versus $\omega^{-1/2}$. Such a plot will have an intercept of I_{kin}^{-1}, and a slope of β^{-1}. It is also possible that if the kinetics are slow, then the reaction can occur within the pores of the catalyst rather than the just on the top surface exposed to the bulk solution, thus increasing the active surface area at slower kinetics and affecting the slope. Using the data presented in Fig. 14, Koutecky–Levich plots were constructed for voltages of 0.6–0.0 vs. NHE, as shown in Fig. 15. The intercept is much greater than 0 at the highest voltages, indicating that kinetic limitations are still present (allowing for a larger active area) at 0.4 V and above. Moreover, the slope is much lower at 0.4 V and above in the plot, indicating a higher active surface area because of reduction within the catalyst pores. However, the plots for 0.0–0.2 V are parallel, indicating that the surface area and other parameters, including the number of electrons per mole of oxygen reacting, remain constant between these voltages. These lines all intercept the y-axis at approximately 0, indicating that kinetic limitations are no longer a factor at these voltages.

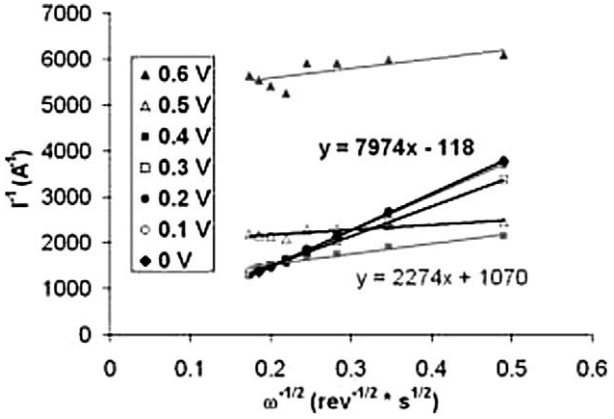

Fig. 15. Koutecky–Levich plots for 2% Fe/VC treated for 2 h at 900 °C in acetonitrile: (▲) 0.6 V, (△) 0.5 V, (■) 0.4 V, (□) 0.3 V, (●) 0.2 V, (○) 0.1 V, and (◆) 0.0 V vs. NHE.

This method can provide an estimate of the number of electrons being transferred in the reaction based on the slope of the Koutecky–Levich plots for voltages where mass transfer is limiting. Based on our calculations, n is >3.8 in this region, and thus the nonnoble metal catalyst appears to be converting a high percentage of O_2 to water. All things considered, this method provides only a rough estimation of n. The rotating ring-disk electrode testing technique is better suited for studying the extent of the conversion of O_2 to H_2O_2, and will be used in the next phase of this study. Nonetheless, these estimates of n show that this catalyst can facilitate complete reduction of O_2 without Pt, in agreement with previous research conducted on similar materials [10].

4. Conclusion

Active ORR catalysts in the form of nitrogen-containing carbons were prepared by the pyrolysis of acetonitrile over a series of Vulcan carbon and metal-doped Vulcan carbon supports. The Fe-doped supports were the best precursors for active ORR catalysts, having greater amounts of nitrogen-containing carbon, higher surface areas, and better catalytic activity compared with Ni-doped and nondoped samples subjected to the same treatment. The iron samples also had higher pyridinic nitrogen content than Ni-doped and nondoped samples, likely resulting from the formation of carbon nanostructures with significant edge plane exposure. This hypothesis agrees with the conclusions of Maldonado and Stevenson, who studied oxygen reduction activity in basic to neutral electrolytes of iron(II) pthalocyanine pyrolysis products [19] and fibers grown using floating iron particles [18]. Pyridinic nitrogen itself may not be the active site for the ORR, but may be a marker for edge plane exposure. Therefore, XPS can possibly give a qualitative measure of edge plane exposure for nitrogen-containing carbons, assuming no other nitrogen species present and no additional influence on the formation of quarternary versus pyridinic nitrogen during carbon growth. Based on these insights into the role of nanostructure, there is a large potential for improvement in ORR activity of nonnoble metal materials considering the advancements being made in the formation of carbon nanostructures.

The most active nonnoble metal catalysts have sufficiently high surface area and conductivity to be considered useful in PEM fuel cell gas diffusion electrodes. The presence of iron contamination in all samples means that we cannot unequivocally say that iron is not part of the ORR active site; however, a more fundamental ongoing study is focusing on the growth of fibers from high-purity chemically removable supports, with high-surface area nitrogen-containing carbon samples being prepared without iron contamination for activity testing and in a more easily characterized form.

Acknowledgments

Financial support for this research was provided by the National Science Foundation (grants NSF-CTS-0437451 and NSF-DGE-0221678). Financial support for equipment through NSF grant DMR 0114098 and Ohio Department of Development Wright Center of Innovation Program is also gratefully acknowledged. The authors thank Sheldon Shore for helpful discussions.

References

[1] S. Srinivasan, in: O.J. Murphy, S. Srinivasan, B.E. Conway (Eds.), Electrochemistry in Transition: From the 20th to the 21st Century, Plenum, New York, 1992, pp. 577–602.
[2] A.J. Bard, L.R. Faulkner, Electrochemical Methods: Fundamentals and Applications, Wiley, NY, 2001.
[3] H. Jahnke, M. Schonborn, G. Zimmerman, Fortschr. Chem. Forsch. 61 (1976) 133.
[4] E. Yeager, Electrochim. Acta 29 (1984) 1527–1537.
[5] E. Yeager, J. Mol. Catal. 38 (1986) 5–25.
[6] J.A.R. van Veen, J.F. van Baar, K.J. Kroese, Chem. Soc., Faraday Trans. I 77 (1981) 2827.
[7] D. Scherson, A.A. Tanaka, S.L. Gupta, D. Tryk, C. Fierro, Z. Holze, E.B. Yeager, Electrochim. Acta 31 (1986) 1247.
[8] A.L. Bouwkamp-Wijnoltz, W. Visscher, J.A.R. van Veen, E. Boellaard, A.M. van der Kraan, S.C. Tang, J. Phys. Chem. B 106 (2002) 12993.
[9] M.C. Martin Alves, G. Tourillion, J. Phys. Chem. 100 (1996) 7566.
[10] S. Gojkovic, S. Gupta, R. Savinell, J. Electroanal. Chem. 462 (1999) 63–72.
[11] P. Gouerec, A. Biloul, O. Contamin, G. Scarbeck, M. Savy, J. Riga, L.T. Weng, P. Bertrand, J. Electroanal. Chem. 422 (1997) 61.
[12] K. Wiesner, Electrochim. Acta 31 (1986) 1073–1078.
[13] M. Lefevre, J.-P. Dodelet, Electrochim. Acta 48 (2003) 2749–2760.
[14] M. Bron, S. Fletcher, M. Hilgendorff, P. Bogdanoff, J. Appl. Electrochem. 32 (2002) 211.
[15] M. Bron, J. Radnik, M. Fieber-Erdmann, P. Bogdanoff, S. Fiechter, J. Electroanal. Chem. 535 (2002) 113–119.
[16] M. Lefevre, J.P. Dodelet, P. Bertrand, J. Phys. Chem. B 104 (2000) 11238.
[17] M. Lefevre, J.P. Dodelet, P. Bertrand, J. Phys. Chem. B 106 (2002) 8705.
[18] S. Maldonado, K.J. Stevenson, J. Phys. Chem. B 109 (2005) 4707–4716.
[19] S. Maldonado, K.J. Stevenson, J. Phys. Chem. B 108 (2004) 11375–11383.
[20] S. Gupta, D. Tryk, I. Bae, W. Aldred, E. Yeager, J. Appl. Electrochem. 19 (1989) 19.
[21] G. Faubert, R. Cote, D. Guay, J.P. Dodelet, G. Denes, P. Bertrand, Electrochim. Acta 43 (1998) 341.
[22] R. Cote, G. Lalande, D. Guay, J.P. Dodelet, G. Denes, J. Electrochem. Soc. 145 (1998) 2411.
[23] H. Wang, R. Cote, G. Faubert, D. Guay, J.P. Dodelet, J. Phys. Chem. B 103 (1999).
[24] G. Lalande, R. Cote, D. Guay, J.P. Dodelet, L.T. Weng, P. Bertrand, Electrochim. Acta 42 (1997) 1379.
[25] G. Faubert, R. Côté, J.P. Dodelet, M. Lefèvre, P. Bertrand, Electrochim. Acta 44 (1999) 2589.
[26] F. Jaouen, S. Marcotte, J.-P. Dodelet, G. Lindbergh, J. Phys. Chem. B 107 (2003) 1376–1386.
[27] S. Ye, A.K. Vijh, Electrochem. Commun. 5 (2003) 272–275.
[28] M.C. Lefebvre, US, 2003.
[29] V.V. Strelko, N.T. Kartel, I.N. Dukhno, V.S. Kuts, R.B. Clarkson, B.M. Odintsov, Surf. Sci. 548 (2004) 281–290.
[30] V.V. Strelko, V.S. Kuts, P.A. Thrower, Carbon 38 (2000) 1499–1525.
[31] A. Montoya, J. Gil, F. Mondragon, T.N. Truong, Fuel Chem. Division Preprints 47 (2002) 424.
[32] A. Montoya, J. Gil, F. Mondragon, T.N. Truong, Fuel Proces. Technol. 77–78 (2002) 453–458.
[33] J.R. Pels, F. Kapteijn, J.A. Moulijn, Q. Zhu, K.M. Thomas, Carbon 33 (1995) 1641–1653.
[34] K. Stanczyk, R. Dziembaj, Z. Piwowarska, S. Witkowski, Carbon 33 (1995) 1383–1392.
[35] A.N. Buckley, Fuel Proces. Technol. 38 (1994) 165–179.
[36] K. Kinoshita, Carbon, Electrochemical and Physicochemical Properties, Wiley Interscience, New York, 1988.
[37] X. Chu, K. Kinoshita, Mater. Sci. Eng. B 49 (1997) 53–60.
[38] P. Chen, M.A. Fryling, R.L. McCreery, Anal. Chem. 67 (1995) 3112–3115.
[39] K.K. Cline, M.T. McDermott, R.L. McCreery, J. Phys. Chem. 98 (1994) 5314–5319.
[40] N.M. Rodriguez, J. Mater. Res. 8 (1993) 3233–3250.
[41] R.T.K. Baker, Carbon 27 (1989) 315–323.
[42] R.T.K. Baker, M.S. Kim, A. Chambers, C. Park, N.M. Rodriguez, Stud. Surf. Sci. Catal. 111 (1997) 99–109.

[43] N.M. Rodriguez, A. Chambers, R.T.K. Baker, Langmuir 11 (1995) 3862–3866.
[44] H. Terrones, T. Hayashi, M. Munoz-Navia, M. Terrones, Y.A. Kim, N. Grobert, R. Kamalakaran, J. Dorantes-Davila, R. Escudero, M.S. Dresselhaus, M. Endo, Chem. Phys. Lett. 343 (2001) 241–250.
[45] J. Fournier, G. Lalande, R. Cote, D. Guay, J.P. Dodelet, J. Electrochem. Soc. 144 (1997) 218.
[46] T. Nakajima, M. Koh, Carbon 35 (1997) 203.
[47] R. Kvon, G. Il'inich, A. Chuvilin, V. Likholobov, J. Mol. Catal. A: Chem. 158 (2000) 413.
[48] J.C. Groen, L.A.A. Peffer, J. Perez-Ramirez, Microporous Mesoporous Mater. 51 (2002) 75–78.
[49] C. Park, M.A. Keane, J. Colloid Interface Sci. 250 (2002) 37–48.
[50] J. Casanovas, J.M. Ricart, J. Rubio, F. Illas, J.M. Jimenez-Mateos, J. Am. Chem. Soc. 118 (1996) 8071–8076.
[51] R. Jiang, F.C. Anson, J. Electroanal. Chem. 305 (1991) 171.